This article has been accepted for inclusion in a future issue of this journal. Content is final as presented, with the exception of pagination.



# MEO SAR: System Concepts and Analysis

Jalal Matar, Marc Rodriguez-Cassola, Gerhard Krieger, *Fellow, IEEE*, Paco López-Dekker, *Senior Member, IEEE*, and Alberto Moreira, *Fellow, IEEE*

***Abstract*— Existing microwave remote sensing instruments used for Earth observation face a clear tradeoff between spatial resolution and revisit times at global scales. The typical imaging capabilities of current systems range from daily observations at kilometer-scale resolutions provided by scatterometers to meter-scale resolutions at lower temporal rates (more than ten days) typical of synthetic aperture radars (SARs). A natural way to fill the gap between these two extremes is to use medium-Earth-orbit SAR (MEO-SAR) systems. MEO satellites are deployed at altitudes above the region of low Earth orbits (LEOs), ending at around 2000 km and below the geosynchronous orbits (GEOs) near 35 786 km. MEO SAR shows a clear potential to provide advantages in terms of spatial coverage, downlink visibility, and global temporal revisit times, e.g., providing moderate resolution images (some tens of meters) at daily rates. This article discusses the design tradeoffs of MEO SAR, including sensitivity and orbit selection. The use of these higher orbits opens the door to global coverage in one- to two-day revisit or continental/oceanic coverage with multidaily observations, making MEO SAR very attractive for future scientific missions with specific interferometric and polarimetric capabilities.**

***Index Terms*— Coverage, medium-Earth-orbit (MEO) synthetic aperture radar (SAR), orbits, SAR, space radiation, system performance.**

## I. Introduction

REMOTE sensing instruments operating in the microwave region play an important role as imaging sensors for a wide variety of applications because of their ability to operate in day or night periods and under severe weather conditions. Key elements in the design of a mission for a specific application include the spatial and temporal resolution of the observation. These two elements have been a matter of tradeoff, where the improvement of one is typically made at the expense of the other. This relation is dictated by the system in use, the viewing geometry, and the covered swath. Examples of current systems include scatterometers operating in low Earth orbits (LEO) and providing high temporal resolutions (1–3 days) at low spatial resolutions (10–50 km) while covering wide swaths (1000–1400 km), or LEO synthetic aperture radar (LEO-SAR) instruments providing high spatial resolutions (1–10 m) at low temporal resolutions (8–16 days) while covering moderate swaths (up to 500 km). Fig. 1 shows these systems on a virtual 2-D temporal–spatial sampling scale. Current LEO-SAR constellations such as Sentinel-1 [1], COSMO-SkyMed [2], or TerraSAR-X/TanDEM-X/PAZ [3]–[6] provide moderate temporal sampling. They are, however, not sufficient for applications that require high temporal and moderate spatial resolutions such as deformation monitoring, soil moisture estimation, sea ice monitoring, or ocean sensing. MEO-SAR systems appear as perfect candidates for this, operating between lower and higher altitude orbits (e.g., geostationary). They can provide moderate single-look resolutions (around 50 m) or alternatively multi-looked imagery with around 500-m resolutions. The increase in the system altitude is exploited to cover wide swaths, 4–5 times larger than wide-swath LEO-SAR systems, with a smaller range of look and incident angles. This reduces the sensitivity to ambiguities and provides a more homogeneous performance along the covered swath. If desired, MEO SAR can also deliver high-resolution imaging over narrow swaths with a reasonable system configuration, as will be shown in Section III.

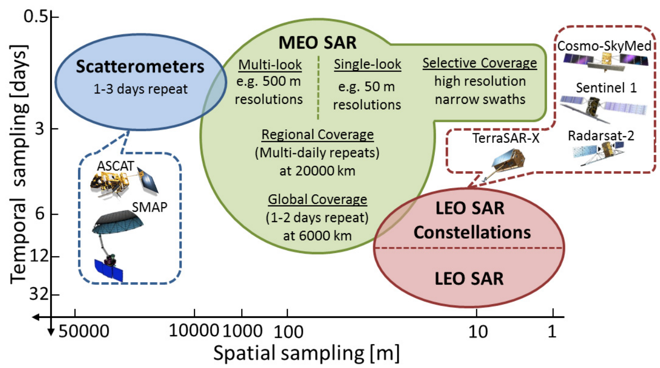


Fig. 1. Spatial versus temporal resolution distribution of current active microwave imaging remote sensors, and the suggested MEO-SAR systems to fill the spatial–temporal resolution gap.

Fig. 2 shows the increased accessible swath with altitude by comparing a LEO system at 693 km (blue/dark) to two exemplary MEO systems, one at 5952 km (turquoise/medium light) with global coverage capabilities and another at 20 182 km (green/light) with the multidaily continental/oceanic coverage capability (e.g., Europe), assuming a constant [20°–47°] incident angle range. The simultaneous coverage of the accessed swaths with LEO-SAR-like resolutions and acceptable

Manuscript received February 1, 2019; revised May 23, 2019 and August 14, 2019; accepted August 23, 2019. *(Corresponding author: Jalal Matar.)*

J. Matar, M. Rodriguez-Cassola, G. Krieger, and A. Moreira are with the Microwave and Radar Institute, German Aerospace Center (DLR), 82334 Weßling, Germany (e-mail: jalal.matar@dlr.de).

P. López-Dekker is with the Delft University of Technology, 2629 HS Delft, The Netherlands.

Color versions of one or more of the figures in this article are available online at http://ieeexplore.ieee.org.

Digital Object Identifier 10.1109/TGRS.2019.2945875

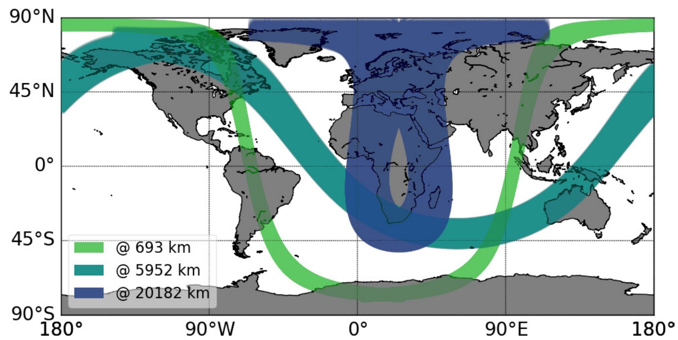


Fig. 2. Visualization of the potential to increase the swath width, for one satellite revolution and a constant incident angle range of [20°–47°], at different altitudes: 693 km (LEO), 5952 km (MEO), and 20 182 km (MEO).

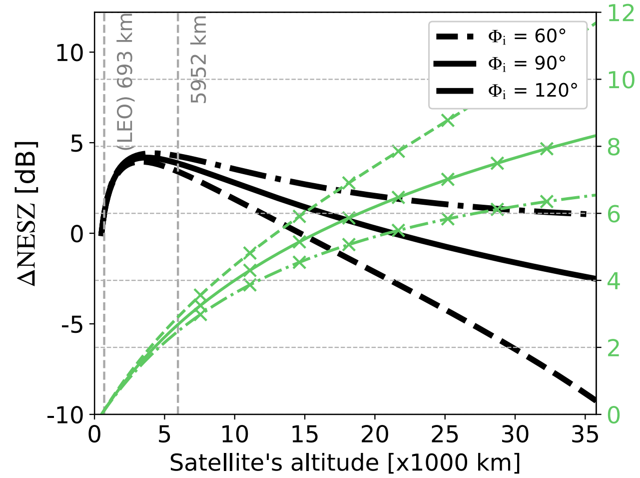


Fig. 3. NESZ variation (thick curves belonging to the left axis) and antenna length variation (labeled with "×" signs and belonging to the right axis) with altitude for the full utilization of $\Delta F_a$. Both variables are plotted with respect to a reference height of 500 km and three different orbital inclinations $\Phi_i$. A constant swath, i.e., $\Delta W_s = 0$ dB, a 0° latitude, and 30° incidence are assumed in the calculation of the plotted data.

sensitivity poses, at the current level of technology, a fundamental challenge for MEO-SAR systems. Following the available literature [7]–[10], this article provides a discussion on the relevant changes experienced by a SAR system at MEO altitudes, showing MEO SAR qualifies to operate at moderate resolutions (tens of meters) with good sensitivity values.

The structure of this article is as follows. Section II discusses the orbit selection, including the tradeoffs imposed by sensitivity, revisit, coverage, radiation environment, and launcher capacity. Section III provides an example of a MEO-SAR mission, comparable to Sentinel-1 in terms of spatial resolution and sensitivity, at around 6000 km with specific interferometric capabilities. This article is closed with an outlook.

## II. Orbit Selection Strategy

The selection of the orbit plays a central role in the design of a remote sensing mission, with implications on sensitivity, revisit, coverage, spacecraft design, and launch. In this section, we analyze the specific tradeoffs imposed by the orbit in the case of MEO-SAR missions.

### A. Imaging and Sensitivity Considerations

The variation (in dB) of the noise equivalent sigma zero (NESZ) with altitude, assuming a constant average transmit power and resolution, and an implicit growth in antenna surface can be approximated by

$$\Delta\mathrm{NESZ} \approx \Delta R + \Delta v_s + 2\cdot\Delta F_a + 2\cdot\Delta W_s \tag{1}$$

where $\Delta R$ and $\Delta v_s$ represent the changes in the slant range and spacecraft velocity with altitude, respectively. $\Delta F_a$ represents the change in the ratio between the ground and spacecraft velocities, whereas $\Delta W_s$ accounts for any desired change in the swath width. The derivation of (1) is presented in the Appendix. Note the condition of constant resolution allows for the growth of the antenna length with altitude ($\Delta L_a = -\Delta F_a$). At higher altitudes, however, this growth may be limited by technological reasons and using spaceborne antennas with lengths/diameters larger than say 30 m is likely to be challenging in terms of weight, size (fairing capacity), and mechanical stability [11].

The factors $\Delta v_s$ and $2\cdot\Delta F_a$, which are both negative, compensate partially for the worsening in the NESZ caused by $\Delta R$ and $2\cdot\Delta W_s$ at higher orbital altitudes. Following the discussion above, the two main potential ways of operating MEO-SAR systems are the following.

1) A LEO-like resolution and swath width (i.e., $\Delta W_s = 0$), with a wider access area and an increase in the average transmit power when needed.
2) An extended swath width covering the complete available access area and a moderate resolution, which helps compensate for the sensitivity loss (a direct consequence of the wider swaths).

In our opinion, the advantages of the latter operation strategy are more easily recognizable than those of the former when compared to current and future LEO SAR counterparts.

Fig. 3 shows the $\Delta$NESZ evaluated at 30° incidence for three different inclinations (60°, 90°, and 120° shown as dashed, solid, and dashed-dotted, respectively) as a function of the orbital altitude compared to a reference orbit at 500 km for a system example with no swath extension (i.e., $\Delta W_s = 0$).

A quick analysis of the results shows that going to orbital altitudes beyond 15 000 km, while covering a LEO-like swath size, is better in terms of NESZ if no limits on the growth of the antenna length are considered. The three ascending curves (marked with "×" signs) corresponding to the right axis of Fig. 3 show this growth in decibels, i.e., $\Delta L_a$, for a constant azimuth resolution. To achieve a 5-m resolution from 500-km altitude, we need roughly a 10-m-long antenna. The same resolution requires spaceborne antennas longer than 30–40 m at altitudes beyond 15000 km, likely very challenging with the current technology. If the increase in the antenna size is limited for practical reasons (i.e., it does not mirror $\Delta F_a$), the factor $2\cdot\Delta F_a$ in (1) needs be substituted by $-2\cdot\Delta L_a$, resulting in an additional loss of sensitivity. Note, however, that this loss is accompanied by an improvement of the azimuth resolution.

This article has been accepted for inclusion in a future issue of this journal. Content is final as presented, with the exception of pagination.



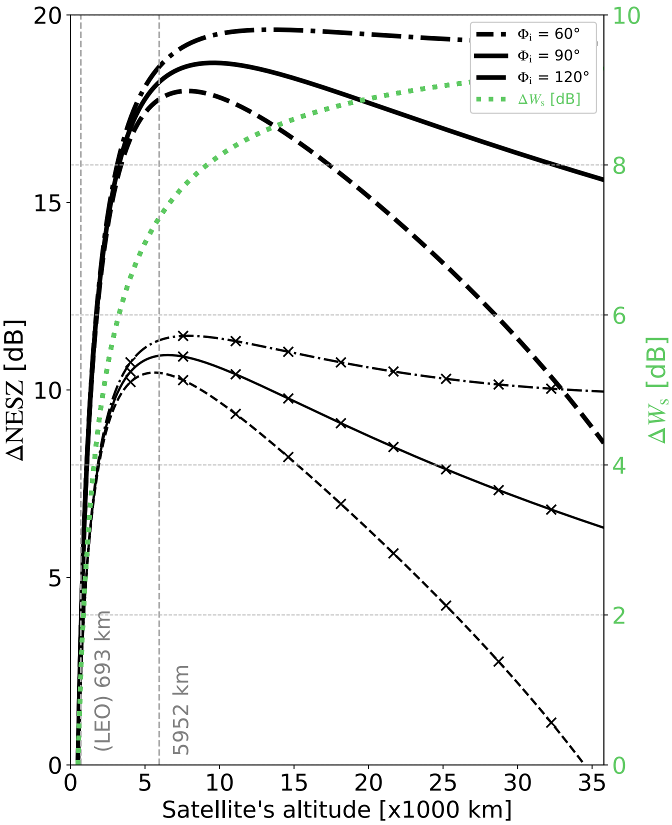


Fig. 4. NESZ variation with altitude for a constant transmit power (thick black curves), or assuming power compensation for increased swath (thin black curves labeled with "×" signs), with respect to a reference height of 500 km and three different orbital inclinations $\Phi_{\text{i}}$. The increase in the swath (light green dotted curve belonging to the right axis) with altitude, i.e., $\Delta W_{\text{s}}$, corresponds to covering a constant incident angle range [20°–47°]. A 0° latitude is assumed for the estimation of the plotted data.

The three thick black curves in Fig. 4 show for the same inclinations the variation of the NESZ as a function of the orbit height assuming an increase of the available swath to the full access area, i.e., the swath width has been extended to cover the increased access area at higher altitudes for the same observation geometry, i.e., a constant range of incident angles (here from 20° to 47°). As in the previous case, the reference orbit height is 500 km. The coverage of the complete accessible swath ($\Delta W_{\text{s}} \neq 0$) results in an approximate 15-dB loss in sensitivity from a 693-km LEO to a 5952-km MEO. However, the higher altitude systems here are providing wider swaths, represented by $\Delta W_{\text{s}}$ (light green dotted curve) on the right axis of Fig. 4 while maintaining the same resolution and average transmit power. The three thin curves (labeled with "×" signs) of Fig. 4 show the reduction in the sensitivity loss if a constant average power per resolution cell, i.e., a constant power density on ground, is assumed. This reduces the sensitivity loss by a factor $-\Delta W_{\text{s}}$, approximately 9 dB from a 693-km LEO to a 5952-km MEO (the 6-dB difference relates to a factor 4 increase in the swath width). The pulse repetition frequency (PRF) also changes with altitude ($\Delta\text{PRF} = \Delta v_{\text{s}} - \Delta L_{\text{a}}$), which requires an equal and opposite increase in the chirp duration if the peak transmit power is to be kept constant for the constant average transmit power.

The conclusion is clear: MEO SAR typically offers an increase in access area and improved revisit, at the cost of a relevant sensitivity loss. If a MEO-SAR system is to be operated with a high resolution over swaths comparable to those covered by LEO systems, which might be an interesting option for applications such as disaster monitoring, the sensitivity loss is minor for low MEO altitudes (below 15 000 km) and can be easily compensated by an increase in the transmit power. Beyond this height, any gain or loss in sensitivity is linked to a growth in the antenna length, which is likely bounded by available technology (e.g., probably reflector antennas of about 30 m may be regarded as a reasonable estimate). If a MEO-SAR system is operated covering a swath close to its access area, a higher sensitivity loss is experienced, which can be compensated with transmitted power or resolution. Typical values of average transmit power are in the order of some (few) kilowatts. The range resolution is somewhat coupled to the azimuth resolution from the design perspective. Any reduction by a factor of two in range resolution provides roughly 3 dB in terms of sensitivity. The gain in azimuth resolution is limited by the antenna size, which is again bounded by current technology. Further possibilities to improve the power budget include the use of higher antennas for illuminating portions of the swaths in transmission or reception. The latter include systems with SCan-On-REceive (SCORE)/SweepSAR capabilities (see [12]–[15]), while the former include the use of burst operation modes [e.g., ScanSAR and terrain observation with progressive scan (TOPS)] or multiple beam antenna technologies (see [16]–[18]).

Other factors that might have an impact on the radar echoes include radio frequency interferences (RFI) and atmospheric propagation. Their effects are, however, well understood by the SAR community based on the available experience on LEO and geosynchronous orbits (GEO) SAR, see [19]–[22], and are not considered as limiting factors for MEO-SAR missions.

### *B. Optimal Orbit Selection*

*1) Orbit Mechanics:* We focus our analysis on repeat ground-track (RGT) orbits [23], which allow the users to perform and schedule measurements systematically. Sun-synchronous repeat orbits are a special case of RGT orbits, in which the precession rate of the orbit is equal to the mean motion of the Earth around the Sun. The orbital precession rate is proportional to the ratio of its inclination to its orbital altitude; hence, in order to maintain the ratio constant for achieving sun-synchronicity, the inclination is increased with altitude [24]. For low MEO altitudes below 6000 km, sun-synchronous orbits exist with increasing inclinations, which may pose a limitation to deliver global coverage, but provides the observation geometry with sensitivity to North–South displacements. This is, in our opinion, one of the major singularities of MEO-SAR systems, which opens the door to true 3-D deformation measurements, a feature that typically requires at least two spacecraft in LEO systems [25]. Beyond 6000 km, sun-synchronous orbits do not exist anymore. Operating in a non-sun-synchronous RGT orbit provides flexibility with respect to the choice of the inclination (if polar coverage is not the target); hence, a choice can be made with

This article has been accepted for inclusion in a future issue of this journal. Content is final as presented, with the exception of pagination.



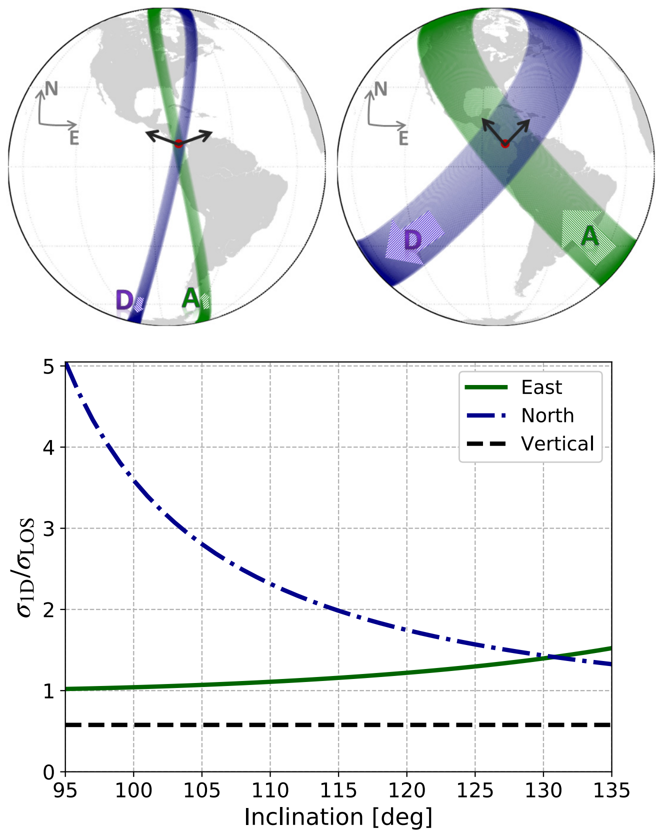


Fig. 5. Projection of the LOS on the ground, represented by the black arrows, for a sun-synchronous LEO at 693 km (top left) and a repeat MEO with 122° inclination at 5952 km (top right). The green (labeled with an A) and blue (labeled with a D) swaths correspond to the right-looking ascending and descending satellite passes, respectively. The plot at the bottom represents the impact of changing the inclination on the achievable 3-D accuracy for an incident angle of 30° near the equator. $\sigma_{1D}$ represents the deformation accuracy along a certain direction, e.g., Easting, Northing, or Vertical, whereas $\sigma_{LOS}$ represents the deformation accuracy along the LOS.

respect to the total coverage, revisit time, and, if desired, the 3-D measurement accuracy. The black arrows in Fig. 5 show the projections of the line-of-sight (LOS) vectors on to the ground for each of the ascending and descending passes of two right-looking SAR satellite, one LEO satellite at 693 km (top left) and another MEO satellite at 5952 km (top right). The top-right plot illustrates the ability of a highly inclined MEO, here 122°, to provide better conditioned observation geometry compared to a near-polar sun-synchronous LEO with 98.15° (top left). As shown in the figure, the projected LOS vectors have similar magnitudes in both the North and East directions in the MEO case, whereas they have a very small Northing component in the LEO case. The bottom plot of Fig. 5 shows the changes in the 1-D deformation accuracy with inclination, where the Northing accuracy approaches that of the Easting and Vertical for higher inclination values. The convergence region in the plot, where all three displacement components are in the same order of magnitude (here at an inclination of around 130°), is of high interest for monitoring land deformations and hazards, because it allows for true 3-D deformation measurements using one satellite only. Unlike a LEO-SAR system, a MEO-SAR system has the potential

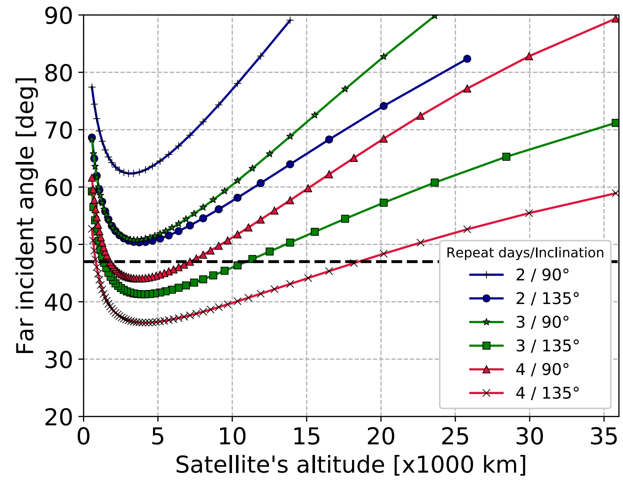


Fig. 6. Far-range incident angles required for equatorial coverage with different repeat cycles and inclinations of RGT orbits, and a 20° near incident angle (single track only: ascending or descending). Black dotted line: 47° far incident angle.

to maintain its global coverage capabilities even under high inclinations, benefiting from the larger access areas at higher altitudes. The calculations of the 3-D accuracy in Fig. 5 are for a target area near the equator, here 8° latitude, observed with a 30° incident angle from the ascending and descending passes of the satellite over the target area. Non-sun-synchronous RGT orbits are subject to periods of orbital days with a difference in the order of few minutes compared to a civil day, causing systematic shifts in the acquisition times. Whether this might introduce relevant systematic components in the physical phenomena under observation should be the matter of a detailed analysis for the MEO-SAR mission under consideration.

*2) Coverage:* If global coverage is the target, suitable candidate orbits can be found based on the required repeat duration, orbital inclination, orbital altitude, and incident angle range. All of the above factors are driven by the user application requirements. For instance, a frequent revisit is desired for disaster monitoring, a high orbital inclination is required for a better 3-D accuracy, orbital altitude can relate to the coverage, radiation, and available launcher capability, whereas the incident angle range relates to the region where the data collected is still useful for all the applications driving the SAR mission. Fig. 6 shows the far incident angle required for achieving equatorial coverage within different repeat days and orbital inclinations, assuming a near incident angle of 20° (with 1 track: ascending or descending). The polar inclinations of 90° and the retrograde inclinations (here 135°) provide the upper and lower limits for the required incident angle, respectively. Prograde orbits with inclinations below 90° rotate in the same direction as the Earth, exhibiting lower Earth-centered-Earth-fixed (ECEF) velocities compared to retrograde orbits, and hence providing less coverage and requiring a bigger range of incident angles for equatorial coverage. The far incident angle corresponding to such orbits would actually fall in between the polar and retrograde curves shown in Fig. 6.

For example, a mission with an incident angle requirement of [20°, 47°] needs at least 3 days (ascending or descending track) in order to achieve equatorial coverage,

This article has been accepted for inclusion in a future issue of this journal. Content is final as presented, with the exception of pagination.



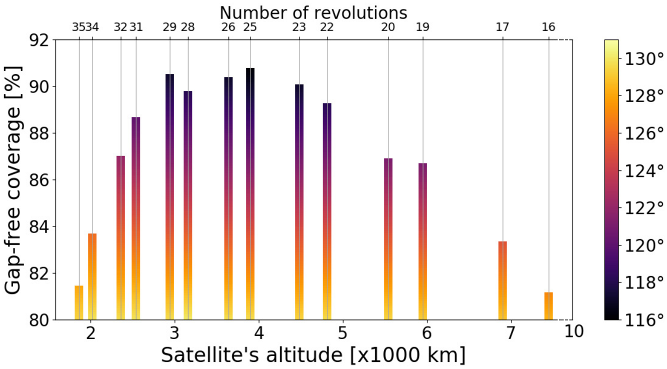


Fig. 7. Gap-free coverage percentage (including land and oceans) with the corresponding orbital inclinations provided by 3-day RGT orbits for [20°–47°] incidence (ascending track—right looking).

while using inclined orbits within the orbital altitude window [1500 km, 10 000 km]. Fig. 7 shows the gap-free coverage percentage $\mathrm{Cov_{gf}}\%$ provided by all 3-day RGT orbits that are capable of covering more than 80% of the entire globe (oceans and continents) in the altitude window [1500 km, 10 000 km] with the ascending track only. The gap-free coverage percentage is calculated as

$$\mathrm{Cov_{gf}}\% = \frac{\text{Earth surface area [latitude range w/o gaps]}}{\text{Earth surface}} \quad (2)$$

where "Earth surface area [latitude range w/o gaps]" represents the area of the Earth surface that is completely covered (without any gaps) between two latitudes. For example, the RGT orbit shown in Fig. 14 provides a gap-free coverage within the latitude block [−46°, 82.5°]. On the other hand, sun-synchronous orbits provide us with a limited number of orbits delivering global coverage, because of the inclination dependence on altitude. Fig. 8 shows all sun-synchronous RGT orbits that are capable of providing more than 80% coverage of the whole globe with a 6-day maximum repeat cycle. The coverage percentage in the plot does not imply a gap-free coverage block. The only orbits capable of providing gap-free coverage are those falling on the upper envelope of the plots (here aligning with the 6-day RGT orbits line for altitudes higher than 800 km). The rest of the orbits require a larger incident angle range in order to avoid the small gaps between consecutive swaths. Releasing the orbital selection from sun-synchronicity conditions removes the dependence of the inclination, eccentricity, and altitude on the Earth's mean motion around the Sun, thus providing a bigger selection of orbits at different altitudes for any repeat cycle, see Fig. 7. This might be necessary at certain MEO altitudes, especially as the orbital choice is also linked to the radiation environment (discussed later in Section II-B3).

An extra measure to aid in the selection of a suitable orbit is the coverage rate, which is defined as the product of the accessible swath, for a certain incident angle range, by the satellite's ground velocity. The change in the coverage rate is defined as

$$\Delta\mathrm{Cov} = \Delta \int_{r_\mathrm{n}}^{r_\mathrm{f}} v_\mathrm{g}(r)dr \quad (3)$$

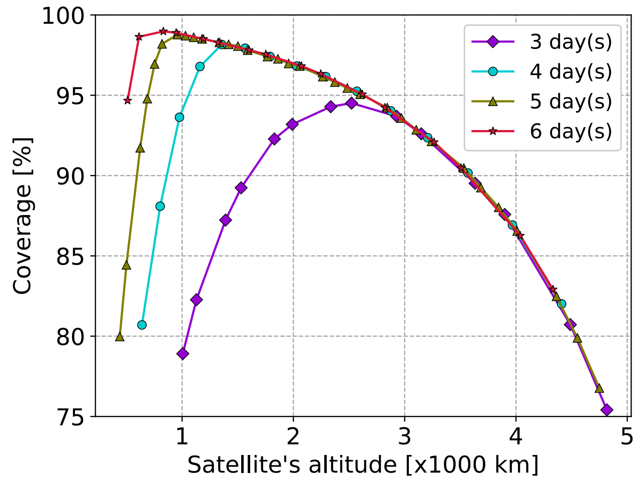


Fig. 8. Coverage percentage with 3, 4, 5, and 6-days RGT sun-synchronous orbits and [20°–47°] incidence (ascending track—right looking).

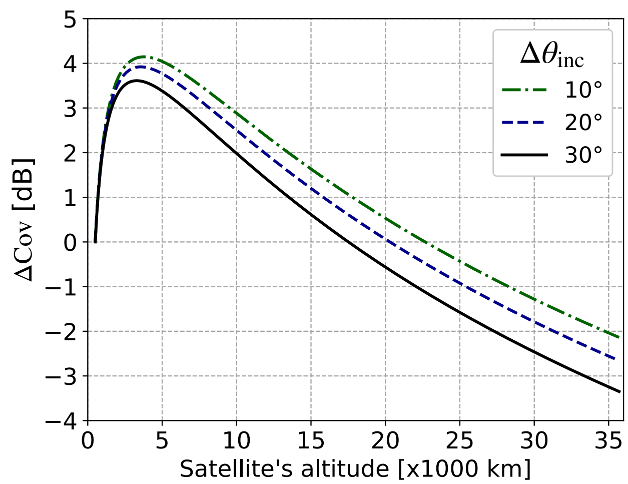


Fig. 9. Variation in the coverage rate ΔCov with altitude at different incident angle ranges, with respect to a reference height of 500 km and a near incident angle of 20°. A 90° inclination and 0° latitude are assumed for the estimation of the ground velocities.

where $r_\mathrm{n}$ and $r_\mathrm{f}$ are the near and far ground ranges, respectively. Fig. 9 shows that orbital altitudes around 3500 km are the most efficient in terms of coverage rate. These altitudes are best suited for missions demanding short repeat cycles and global coverage, see Fig. 7; however, they are subject to high radiation environments. On the other hand, the coverage rate at orbital altitudes beyond 17 000 km is lower than that of a LEO orbit at 500 km, making such orbits better suited for local coverage where wide accessible swaths and short repeat cycles are more valued. MEO can provide local continental coverage within 1 day. As an example, the "1/2 RGT" orbit at about 20 000 km repeats twice a day and covers Europe with a [20°–45°] incidence. Fig. 10 shows that increasing the incident angle range in a "1/2 RGT" orbit to [20°–60°] provides complete coverage of the North and South poles, in addition to certain continents and oceans with daily revisit. At similar heights, it is possible to design missions covering other continents or oceans with twice a day revisit. The choice of the optimal orbit is then a matter of tradeoff between the coverage rate for a certain repeat requirement, the corresponding

This article has been accepted for inclusion in a future issue of this journal. Content is final as presented, with the exception of pagination.



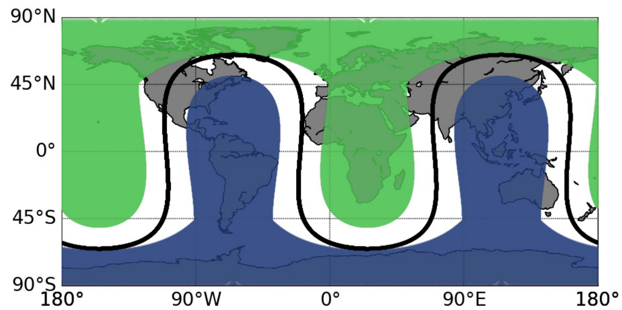


Fig. 10. Coverage from a 1/2 RGT orbit with an inclination of 65° at 20182 km for an access range of [20°–60°]. The black line is the ground track of the satellite and the light green and dark blue swaths correspond to left- and right-looking geometries, respectively.

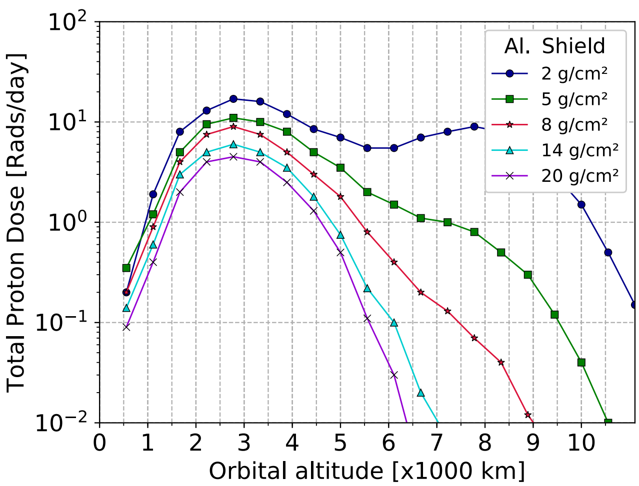


Fig. 11. Projected proton dose rate for 90° orbital inclinations as a function of aluminum shield thickness (AP-3, E > 50 MeV) [28].

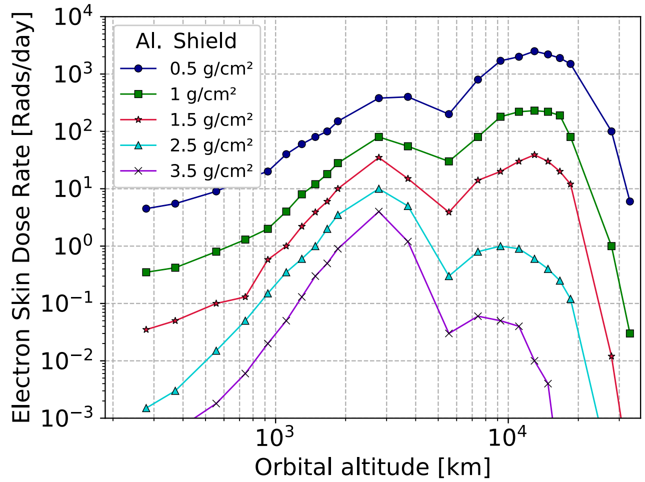


Fig. 12. Projected electron skin dose rate for 90° orbital inclinations as a function of aluminum shield thickness (1968, E > 0.5 MeV) [28].

sensitivity loss, the radiation environment, and the requirements imposed on gap-free coverage, i.e., tolerance for gaps. Sun-synchronicity is an additional factor if the coverage demands can be achieved within the repeat requirements, as shown in Fig. 8.

*3) Radiation and Shielding Costs:* Space radiation, specifically, ionizing radiation, can cause serious damage to payload electronics. For the altitude window [1500 km–10 000 km], we have a major radiation contribution of the inner Van Allen belt starting at the top of the atmosphere at around 500 km and ending at around 6500 km with a peak radiation at around 3500 km, and a minor contribution of the outer belt whose radiation peak is at around 19 000 km. The inner belt is occupied mostly by highly charged protons, whose flux densities are higher for 0° inclinations and lower for polar orbits [26]. The highest priority at low MEO altitudes is to shield against protons whose energies are higher than 50 MeV since those are harder to stop in an aluminum shield than lower energy protons or electrons [27]. Fig. 11 shows that using an increased aluminum shield thickness from 2 to 8 g/cm$^2$, above 5500 km, can reduce the total proton dose to LEO-like levels. The increase in weight for shielding a 0.5-m$^3$ cube payload may be of some two to three hundred kilograms, and it is not perceived as a technological challenge for future MEO-SAR missions operating in the low radiation region. For higher MEO altitudes, the outer Van Allen belt dominates and is mostly occupied by high energy electrons and ions. Fig. 12 shows that for electrons with energies greater than 0.5 MeV, an increased shield thickness of 3 g/cm$^2$ can reduce electron skin dose rates to LEO-like levels [28], [29], making shielding less of an issue for a multidaily repeat orbit (1/2 RGT orbit) at 20 000 km.

Combining the study of the radiation environment with the plots in Fig. 9 provides us with two options: operating in maximum coverage rate zones (around 3500 km) and suffer from high radiation, thicker shielding, and lower satellite lifetimes, or operating in low radiation zones with moderate shielding, acceptable coverage rates, and longer satellite lifetimes.

*4) Launch Cost:* The mass-to-orbit capability of a launcher is directly coupled to the launch cost and depends mainly on the latitude of the spaceport, the altitude, and inclination of the target orbit. To estimate the approximate payload mass decrease, we assume that the different orbits are reached by launching from a circular low Earth park orbit, at an altitude $h_{\mathrm{ref}}$, through a Hohman transfer orbit (HTO) to reach the designated circular orbit at an altitude $h_{\mathrm{orb}}$. This transfer, assuming no change in the orbital inclination, requires a velocity increment of

$$\begin{aligned}\Delta V \; &= \sqrt{\frac{\mu}{h_{\mathrm{ref}}+r_{\mathrm{E}}}}\cdot\left(\sqrt{\frac{2\cdot(h_{\mathrm{orb}}+r_{\mathrm{E}})}{h_{\mathrm{ref}}+h_{\mathrm{orb}}+2r_{\mathrm{E}}}}-1\right)\\ &\quad+\sqrt{\frac{\mu}{h_{\mathrm{orb}}+r_{\mathrm{E}}}}\cdot\left(1-\sqrt{\frac{2\cdot(h_{\mathrm{ref}}+r_{\mathrm{E}})}{h_{\mathrm{ref}}+h_{\mathrm{orb}}+2r_{\mathrm{E}}}}\right) \qquad (4)\end{aligned}$$

where $\mu$ is the standard gravitational parameter of the Earth, and $r_{\mathrm{E}}$ is the radius of the Earth [30]. For a constant exhaust velocity $v_{\mathrm{e}}$, the loss of launcher payload mass $\Delta M$ required to achieve a certain velocity increment is defined by Tsiolkovsky [31] as

$$\Delta M = \frac{M_{\mathrm{orb}}}{M_{\mathrm{ref}}} = \exp\left(-\frac{\Delta V}{v_{\mathrm{e}}}\right) \qquad (5)$$

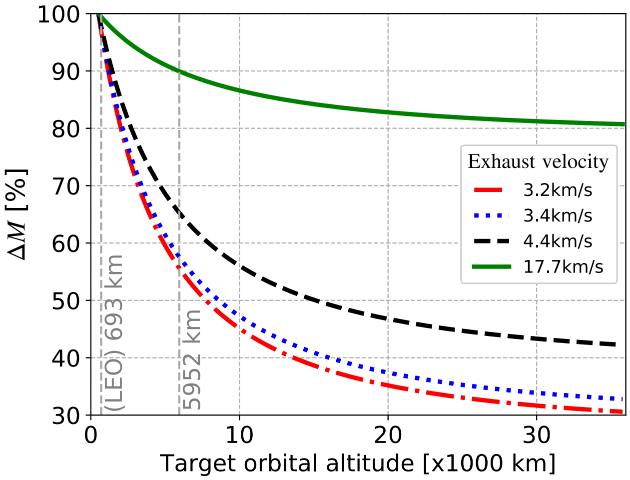


Fig. 13. Reduction in the mass-to-orbit capability of typical launchers for going from a reference low Earth park orbit, here at $h_{\mathrm{ref}} = 400$ km, to higher orbital altitudes within the same orbital plane. 100% is at 512 km (orbital height of TerraSAR-X).

where $M_{\mathrm{ref}}$ is the combined mass of the launcher payload and needed propellants at $h_{\mathrm{ref}}$, and $M_{\mathrm{orb}}$ is the launcher payload mass, i.e., spacecraft mass, arriving at $h_{\mathrm{orb}}$. Fig. 13 shows this loss for launching from a park orbit at 400 km to various orbital altitudes within the same orbital plane, using a single HTO (for chemical thrusters) and different exhaust velocities for typical launchers in vacuum, e.g., Soyuz with $v_{\mathrm{e}} \approx 3.2$ km/s [32], Falcon 9 Merlin 1D with $v_{\mathrm{e}} \approx 3.4$ km/s [33], and Ariane 5 [34] with $v_{\mathrm{e}} \approx 4.4$ km/s. At around 6000 km, we have a 35%–40% mass loss (with chemical propulsion) compared to LEO systems. An extra 4%–6% loss is expected if a 27°–28° orbital inclination change is required (comparing polar to more inclined orbits).

On the one hand, a MEO system faces a decrease in the payload capability of the launcher, and on the other hand, a weight increase is expected for a MEO spacecraft in order to compensate for the sensitivity loss by using larger antennas, thicker radiation shields, larger batteries, and solar panels. However, this payload demand is not considered to be a limiting factor for a MEO mission, especially if we keep in mind the fast evolution of launcher capabilities and reusability modes, in addition to the possibility of using electric propulsion systems, e.g., ion thrusters, that can provide higher exhaust velocities at the cost of a longer transfer time, which further reduces the decrease in the mass-to-orbit capability for going toward higher altitude orbits. This is clearly illustrated in the solid curve in Fig. 13 for an electrically powered thruster with an exhaust velocity of 17.7 km/s, i.e., a specific impulse of 1800 s, which exhibits only 10% mass loss for going to 6000 km compared to LEO systems.

## III. Example MEO-SAR Mission Scenario

In this section, we define an example MEO-SAR mission using the information provided above. To enhance its illustrative power, we compare the resulting mission to a state-of-the-art LEO constellation, namely, ESA's Sentinel-1 [1]. The target of this mission example is to provide a system with similar observation capabilities and incident angle range (i.e., between 20° and 47°) intended for the same range of applications while offering an improved access range and revisit time. The basic characteristics of the system in terms of swath, resolution, sensitivity, and ambiguity rejection are given in Table I. Modes A, B, and C roughly correspond in terms of resolution and sensitivity to the stripmap (SM), interferometric wide swath (IW), and extra wide swath (EW) modes of Sentinel-1 [1]. Mode D corresponds to a full-swath imaging mode covering the entire access range of the system. The authors are aware that the design of a dedicated MEO-SAR mission would benefit from a more systematic approach based on the analysis of mission objectives and user requirements. This is not, however, the purpose of this article, which is focused on the opportunities offered by future MEO-SAR concepts. All things considered, we believe this example offers a simplified way to illustrate the potential and challenges of MEO SAR.

TABLE I
Basic System Requirements for the MEO-SAR Mission Example (à la Sentinel-1) in Different Imaging Modes

| Parameter | Mode A | Mode B | Mode C | Mode D |
|---|---|---|---|---|
| Frequency [GHz] | 5.405 | | | |
| Resolution [m$^2$] ($\delta_{\mathrm{x}} \times \delta_{\mathrm{gr}}$) | 5 × 5 | 20 × 5 | 40 × 20 | - |
| Swath width [km] | >80 | >250 | >410 | - |
| Repeat [days] | < 6 | | | |
| Incidence [deg] | - | - | - | [20, 47] |
| NESZ [dB] | <-22 | | | |
| TASR [dB] | <-25 | | | |

TABLE II
Swath and Repeat for the Different Imaging Modes of the MEO-SAR Mission Example

| Parameter | Mode A | Mode B | Mode C | Mode D |
|---|---|---|---|---|
| Swath width [km] | >80 | >250 | >410 | 1667 |
| Repeat [days] | 3 | | | |

### A. Orbit Selection

We make use of the coverage analysis in Section II-B2 to define a suitable orbit height. According to Fig. 6, global coverage can be achieved with a minimum orbital repeat cycle of three days at heights ranging from 2000 to 10 000 km. Section II-B3 suggests for this desired altitude range an operation outside the radiation peak zone, here beyond 5700 km. According to Fig. 7, the orbit providing the largest gap-free coverage (roughly 86%) is the 3/19 RGT, at 5952 km height and an inclination of 122°. This orbit provides global coverage with a 3-day repeat cycle and a swath width of about 1667 km. Table II gives the updated values of swath and repeat duration for the selected orbit. Fig. 14 shows the ascending coverage map of such an orbit between 20° and 47° incidence, providing enough overlap between consecutive swaths. Note that areas approaching the poles are accessible several times within a cycle.

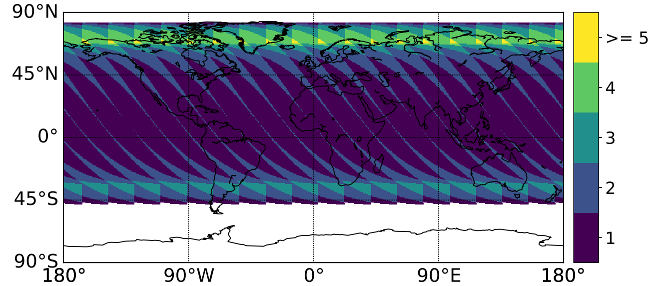


Fig. 14. Ascending coverage from a 3/19 RGT orbit with an inclination of 122° at 5952 km. 86% of the Earth's surface is covered for an access range of [20°–47°] (right looking).

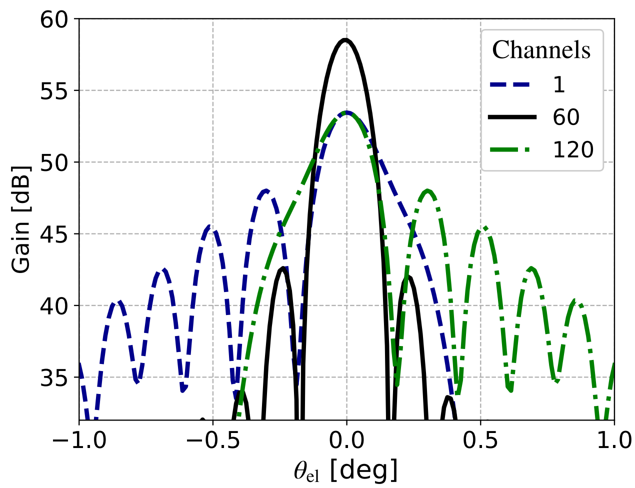


Fig. 15. Antenna pattern defocusing effects on gain and beamwidth for the center and edge channels in elevation (created using GRASP software).

## B. Instrument and Mode Design

In this section, we present the design of the instrument and the imaging modes, fulfilling the basic performance figures outlined in Tables I and II. This can be accomplished by following the discussions in Section II-A. According to (9), the antenna length required to achieve a minimum azimuth resolution of 5 m from a 5952-km orbit is around 22 m. As shown in Fig. 4, mode D providing imaging over the whole access range (i.e., 1667-km swath) needs to overcome a loss in sensitivity of 15 dB with respect to a Sentinel-1 orbital altitude of 693 km. To partially compensate for this loss, a 22-m reflector antenna with SCORE capabilities is designed for this system. As discussed in Section II-A, the remaining loss may be compensated by: 1) using extra transmit power; 2) reducing the 1667-km swath width; or 3) decreasing the resolution. For comparison, Sentinel-1 uses around 370- and 200-W average powers for the SM/IW and EW modes, respectively.

*1) Antenna Design:* To cover the complete incidence range (i.e., [20°, 47°]), the 22-m reflector needs digital steering capabilities in elevation over a span of about 12°. The single-element beamwidth of the 22-m reflector is of about 0.176°. The spacing between elements controls the scalloping in elevation. As an example, spacings of 1.15$\lambda$ and 0.66$\lambda$ result in scalloping values of less than 3 and 1 dB, respectively. We choose for our system the latter, which results in 120 elements in elevation and provides redundancy in case of element failure. The use of SCORE gives extra 6–10 dB gain from the edges to the center of the swath with the existing reflector [12], [14]. The SCORE beams are formed by the complex weighting of a set of neighboring elements. As an example, Fig. 15 shows the defocusing effects on the gain and beamwidth for the edge elements compared to the focused center element. The feed array incorporates two

TABLE III

PARAMETERS OF THE REFLECTOR ANTENNA SUGGESTED FOR THE "3/19 RGT" MEO-SAR MISSION EXAMPLE

| Parameter | Value |
|---|---|
| Diameter | 22 m |
| Focal length | 19.8 m |
| Offset (elevation) | 0 m |
| Frequency | 5.405 GHz |
| Azimuth elements/channels | 2/1 |
| Elevation elements/channels | 120/120 |
| Element spacing | 0.66 $\lambda$ |
| Feed tilt angle | 0° |
| Feed array size | 4.33 m × 0.07 m |
| Feed array mount | 5 m × 1 m |

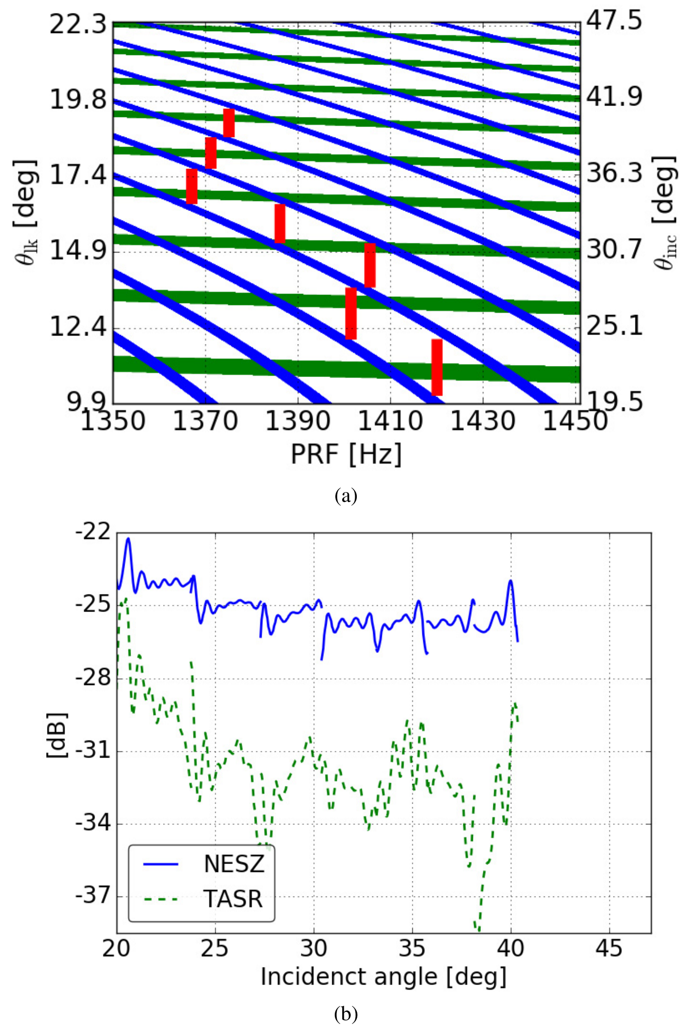


Fig. 16. Mode C. (a) Timing diagram (incident and look angles versus PRF). Green quasi-horizontal stripes represent the nadir echoes, blue oblique stripes mark the transmit events, and red vertical bars correspond to the selected swaths. The duty cycle is 8%. (b) NESZ and TASR.

This article has been accepted for inclusion in a future issue of this journal. Content is final as presented, with the exception of pagination.



TABLE IV
PERFORMANCE VALUES OF THE SUGGESTED "3/19 RGT" MEO-SAR MISSION EXAMPLE IN DIFFERENT MODES

| Parameter | Mode A | Mode B | Mode C | Mode D |
|---|---|---|---|---|
| Imaging mode | stripmap | ScanSAR | ScanSAR | ScanSAR |
| Average power [W] | [300, 575] | 400 | 350 | 350 |
| Total losses [dB] | 4 | | | |
| Total noise temperature [K] | 606 | | | |
| Duty cycle [%] | 8 | | | |
| System bandwidth [MHz] | [43, 87] | [55, 66] | [12, 22] | [11, 22] |
| PRF range [Hz] | [1290, 1418] | [1366, 1404] | [1365, 1419] | [1290, 1418] |
| Resolution ($\delta_x \times \delta_{gr}$) [m$^2$] | 5 × 5 | 20 × 5 | 40 × 20 | 57 × 20 |
| Swath width [km] | [115, 206] | 500 | 1211 | 1667 |
| Incident angles [deg] | [20, 47] | [27.3, 35.6] | [20, 40.3] | [20, 47] |
| NESZ [dB] | <-22 | <-22 | <-22 | <-22 |
| TASR [dB] | <-26 | <-30 | <-25 | <-25 |

azimuth elements combined into a single channel to reduce the crosstalk between polarizations [35], [36]. If needed, additional azimuth elements can be used to collect the energy spread at the edges of the array improving the gain of the edge channels [37]. The feed array can be deployed on a 5 m × 1 m plate, which is expected to cause negligible blockage considering the reflector size. Table III gives the parameters of the suggested antenna design.

*2) Mode Design and Performance:* Considering the antenna developed in Section III-B1, mode A should be an SM mode. More options are possible for modes B, C, and D, including multibeam SM or burst-mode techniques [38]–[40]. Since the purpose of this section is to provide the reader with an example about the feasibility of MEO SAR, we believe the use of ScanSAR as an imaging mode will probably reach a wider audience. The timing diagrams, including a candidate subswath selection for modes C and D, are shown in the top plots of Figs. 16 and 17, respectively. The relaxed timing constraints are a consequence of the smaller look angle ranges required to cover the entire swath at this orbit height. The diagrams show the incident and look angles versus the PRF. The blue oblique stripes represent transmit events with an 8% duty cycle, the green quasi-horizontal stripes represent nadir echoes, and the red vertical bars correspond to the selected ScanSAR bursts for modes C and D. Each of the seven bursts in mode C has been extended in order to fully utilize the gap between transmit events, achieving a total swath of 1211 km for an average power of 350 W. A similar average transmit power is required for mode D, which uses ten bursts to cover the whole access area with a standard ScanSAR imaging mode, resulting in a 57-m azimuth resolution. For the sake of comparison, increasing the average transmit power of mode D up to 1 kW allows for an improvement in the azimuth resolution to roughly 20 m. The increased average power has no implications on the peak power, since the different swaths within each beam are illuminated simultaneously by different feed elements. Mode B is a subset of mode C, where the three middle bursts are used to cover a 500-km swath with the required resolution and an average transmit power of 400 W. Each of the single SM swaths of mode A is also a subset of

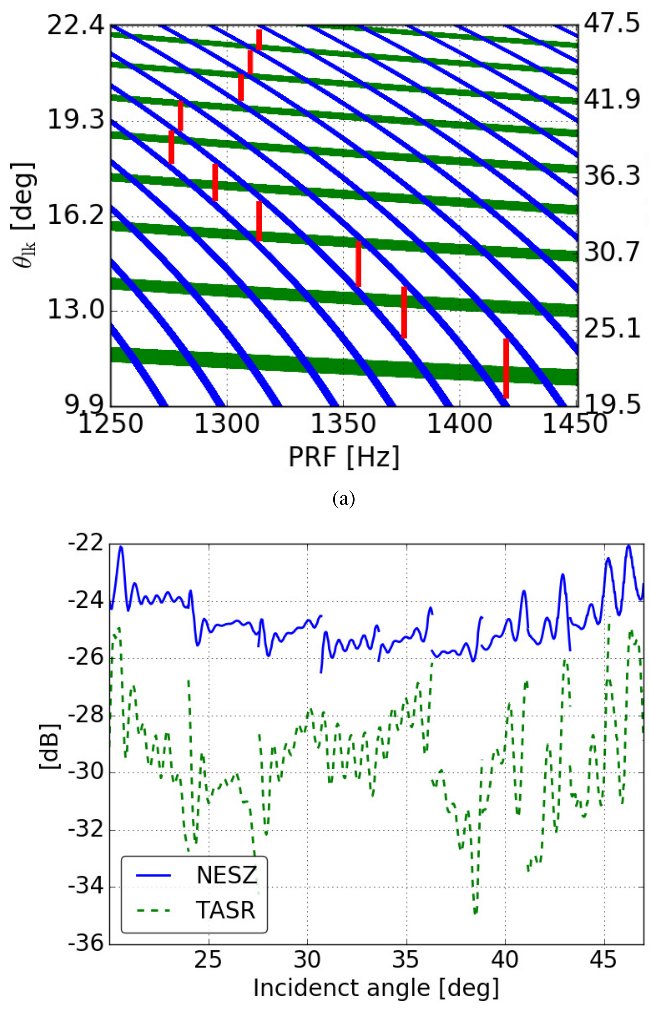


Fig. 17. Mode D. (a) Timing diagram (incident and look angles versus PRF). Green quasi-horizontal stripes represent the nadir echoes, blue oblique stripes mark the transmit events, and red vertical bars correspond to the selected swaths. The duty cycle is 8%. (b) NESZ and TASR.

the different bursts of mode D. The swath widths range from 115 to 206 km based on their locations in the timing diagram. A total average power of 300 W is sufficient for the central swaths, whereas the edge ones require an increase of about

2.8 dB to compensate for the defocusing of the patterns. Note the assumption of perfect nadir echo suppression has been accepted in the definition of the subswaths, a reasonable one given the size of the reflector, and the digital beamforming capabilities of the system. The bottom plots of Figs. 16 and 17 show the corresponding NESZ and total ambiguity-to-signal ratio (TASR) for modes C and D, respectively. The resulting performance of each mode is displayed in Table IV.

### C. Comparison With Sentinel-1

A quick analysis suggests that using a MEO system with a moderate resolution, e.g., mode D with $\delta_x \times \delta_{gr} = 57$ m $\times$ 20 m, and moderate power might be better suited for deformation monitoring tasks or soil moisture estimation than contemporary LEO missions. Compared to Sentinel-1, the MEO system example discussed above offers an increase between 1.5 and 3 times in imaged swath, a revisit of 3 days instead of 12, and sensitivity to the Northing component of the deformation due to the inclination of the orbit, all this for 1–2-dB increase in average power and the usage of a large reflector antenna with SCORE capabilities.

## IV. Conclusion

This article provides a discussion on the relevant tradeoffs to be addressed in the design of a MEO-SAR mission, including orbit, system, and launch aspects. The intrinsic challenge of the MEO-SAR power budget can be overcome if moderate-resolution systems, e.g., in the order of tens of meters, are in view. The analysis also shows the ability of MEO SAR to provide global coverage with 1- to 2-day revisit, or continental/oceanic coverage with multidaily observations, which shows a clear potential for missions targeting land applications such as soil moisture and crop monitoring or polar and oceanic mapping. Moreover, a specific advantage of MEO SAR is the sensitivity to the North–South components of deformation, which, coupled with significantly improved revisit times, opens the door to true 3-D motion and deformation estimates. This feature is hardly available to monostatic LEO systems [25] and is very useful for the monitoring of physical phenomena such as landslides, earthquakes, or volcanic activity.

## Acknowledgment

This article is a research activity within the Microwave and Radar Institute of the German Aerospace Center (DLR).

## Appendix

This section provides the relevant information required for the derivation of ΔNESZ in (1). The general form describing the variation (in dB) of the NESZ with altitude, for a constant system bandwidth and frequency, can be approximated by

$$\Delta\mathrm{NESZ} \approx 3 \cdot \Delta R + \Delta v_s - \Delta P_{avg} - \Delta G_{Tx} - \Delta G_{Rx} \quad (6)$$

where $\Delta R$ and $\Delta v_s$ represent the changes in the slant range and satellite velocity with altitude, respectively. $\Delta P_{avg}$, $\Delta G_{Tx}$, and $\Delta G_{Rx}$ account for any desired changes in the average transmit power, transmit gain, and receive gain, respectively. All factors in (6) are given in decibels with respect to a reference orbital height (e.g., LEO). Let us further expand (6) into purely geometrical terms. The change in the gain, assuming a monostatic system that uses the same antenna for transmit and receive without employing any digital beam forming, is then proportional to the change in the antenna area, that is,

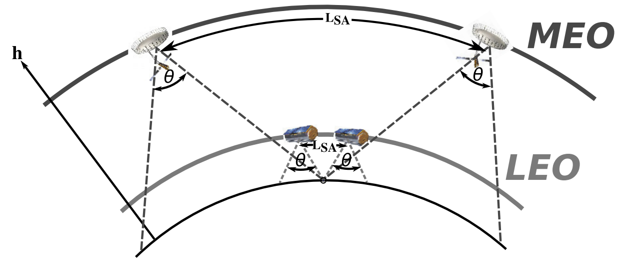


Fig. 18. Qualitative representation of the increase in the synthetic aperture length $L_{SA}$ with altitude $h$ for the same antenna beamwidth $\theta$.

$$\Delta G_{Tx} = \Delta G_{Rx} \approx \Delta L_a + \Delta L_e \quad (7)$$

where $\Delta L_a$ represents the change in the length of the antenna along azimuth and $\Delta L_e$ represents the change in the height of the antenna along elevation. $\Delta L_e$ can be linked to a change in the swath width $\Delta W_s$ in the following manner:

$$\Delta L_e \approx \Delta R - \Delta W_s. \quad (8)$$

If the azimuth resolution is to be maintained, the variation in the length of the synthetic aperture with altitude has to be considered. The curved nature of satellite orbits leads to a reduction in the ratio between the ground and orbital velocities of a spacecraft at higher orbits. This translates into an increase in the length of the synthetic aperture as shown in Fig. 18, which results into a better azimuth resolution for a constant antenna size [41], that is,

$$\delta_x = f(L_a) \cdot \frac{v_g(h, \theta_i, \Phi_i, \theta_{lat})}{v_s(h)} \approx \frac{L_a}{2} \cdot F_a \quad (9)$$

where $f(L_a)$ is approximated by half the length of the antenna, $v_s$ is the spacecraft velocity depending on the orbital altitude $h$, and $v_g$ is the ground velocity that also depends on the incident angle $\theta_i$, the orbital inclination $\Phi_i$, and the latitude of the imaged scene $\theta_{lat}$.

According to (9), a constant azimuth resolution, i.e., $\Delta\delta_x = 0$ dB, can be achieved at higher altitudes using longer antennas (and substitute $\Delta L_a$ by $-\Delta F_a$), which results in a higher antenna gain. Under the assumption of constant average transmit power and resolution, and considering the resulting growth in antenna surface according to (8) and (9), (6) can be easily shown to be equivalent to the expression in (1).

## References

[1] R. Torres *et al.*, "GMES Sentinel-1 mission," *Remote Sens. Environ.*, vol. 120, pp. 9–24, May 2012.

[2] F. Covello *et al.*, "COSMO-SkyMed an existing opportunity for observing the Earth," *J. Geodyn.*, vol. 49, nos. 3–4, pp. 171–180, 2010.

[3] A. Moreira *et al.*, "TanDEM-X: A TerraSAR-X add-on satellite for single-pass SAR interferometry," in *Proc. IEEE Int. Geosci. Remote Sens. Symp.*, vol. 2, Sep. 2004, pp. 1000–1003.

[4] G. Krieger *et al.*, "TanDEM-X: A satellite formation for high-resolution sar interferometry," *IEEE Trans. Geosci. Remote Sens.*, vol. 45, no. 11, pp. 3317–3341, Nov. 2007.

[5] M. Zink *et al.*, "TanDEM-X: The new global DEM takes shape," *IEEE Geosc. Remote Sens. Mag.*, vol. 2, no. 2, pp. 8–23, Jun. 2014.

[6] S. Gantert, A. Kern, R. Düring, J. Janoth, L. Petersen, and J. Herrmann, “The future of X-band SAR: TerraSAR-X next generation and World-SAR constellation,” in *Proc. Asia–Pacific Conf. Synth. Aperture Radar*, Sep. 2013, pp. 20–23.

[7] W. Edelstein, S. Madsen, A. Moussessian, and C. Chen, “Concepts and technologies for synthetic aperture radar from MEO and geosynchronous orbits,” in *Proc. SPIE, Enabling Sensor Platform Technol. Spaceborne Remote Sens.*, vol. 5659, Jan. 2005, pp. 195–203.

[8] A. Moussessian, C. Chen, W. Edelstein, S. Madsen, and P. Rosen, “System concepts and technologies for high orbit SAR,” in *IEEE MTT-S Int. Microw. Symp. Dig.*, Jun. 2005, pp. 1–4.

[9] U. Klein, C. Lin, N. Atkinson, J. Charlton, and C. Philpot, “Future microwave radiometers in geostationary and medium Earth orbit,” in *Proc. IEEE Int. Geosci. Remote Sens. Symp.*, vol. 3, Jul. 2003, pp. 2158–2160.

[10] D. M. Tralli, W. Foxall, and C. Schultz, “Concept for a high MEO InSAR seismic monitoring system,” in *Proc. IEEE Aerosp. Conf.*, Mar. 2007, pp. 1–7.

[11] Harris Corporation,. (2018). Unfurlable Space Reflector Solutions. [Online]. Available: https://www.harris.com/sites/default/files/downloads/solutions/55430_d0 807_unfurlable_space_antenna_solutions_final_el_web.pdf

[12] A. Freeman *et al.*, “SweepSAR: Beam-forming on receive using a reflector-phased array feed combination for spaceborne SAR,” in *Proc. IEEE Radar Conf.*, May 2009, pp. 1–9.

[13] A. Moreira *et al.*, “Tandem-L: A highly innovative bistatic SAR mission for global observation of dynamic processes on the Earth’s surface,” *IEEE Geosci. Remote Sens. Mag.*, vol. 3, no. 2, pp. 8–23, Jun. 2015.

[14] G. Krieger, N. Gebert, and A. Moreira, “Multidimensional waveform encoding: A new digital beamforming technique for synthetic aperture radar remote sensing,” *IEEE Trans. Geosci. Remote Sens.*, vol. 46, no. 1, pp. 31–46, Jan. 2008.

[15] R. Moore, J. Claassen, and Y. Lin, “Scanning spaceborne synthetic aperture radar with integrated radiometer,” *IEEE Trans. Aerosp. Electron. Syst.*, vol. AES-17, no. 3, pp. 410–421, May 1981.

[16] F. De Zan and A. M. Guarnieri, “TOPSAR: Terrain observation by progressive scans,” *IEEE Trans. Geosci. Remote Sens.*, vol. 44, no. 9, pp. 2352–2360, Sep. 2006.

[17] N. Gebert, G. Krieger, and A. Moreira, “Multichannel azimuth processing in ScanSAR and TOPS mode operation,” *IEEE Trans. Geosci. Remote Sens.*, vol. 48, no. 7, pp. 2994–3008, Jul. 2010.

[18] M. Suess and W. Wiesbeck, “Side-looking synthetic aperture radar system,” *Eur. Patent*, vol. 1, no. 241, p. 487, 2002.

[19] J. R. Rodon, A. Broquetas, A. M. Guarnieri, and F. Rocca, “Geosynchronous SAR focusing with atmospheric phase screen retrieval and compensation,” *IEEE Trans. Geosci. Remote Sens.*, vol. 51, no. 8, pp. 4397–4404, Aug. 2013.

[20] A. M. Guarnieri, A. Leanza, A. Recchia, and S. Tebaldini, “Atmospheric phase screen in GEO-SAR: Estimation and compensation,” *IEEE Trans. Geosci. Remote Sens.*, vol. 56, no. 3, pp. 1668–1679, Mar. 2018.

[21] A. Danklmayer, B. J. Doring, M. Schwerdt, and M. Chandra, “Assessment of atmospheric propagation effects in SAR images,” *IEEE Trans. Geosci. Remote Sens.*, vol. 47, no. 10, pp. 3507–3518, Oct. 2009.

[22] Y. Li, A. M. Guarnieri, C. Hu, and F. Rocca, “Performance and requirements of GEO SAR systems in the presence of radio frequency interferences,” *Remote Sens.*, vol. 10, no. 1, p. 82, 2018.

[23] S. Vtipil and B. Newman, “Determining an Earth observation repeat ground track orbit for an optimization methodology,” *J. Spacecraft Rockets*, vol. 49, no. 1, pp. 157–164, 2012.

[24] R. Boain, “AB-Cs of sun-synchronous orbit mission design,” in *Proc. 14th AAS/AIAA Space Flight Mech. Conf.*, 2004, Paper AAS 04-108.

[25] P. Prats-Iraola, P. Lopez-Dekker, F. De Zan, N. Yagüe-Martinez, M. Zonno, and M. Rodriguez-Cassola, “Performance of 3-D surface deformation estimation for simultaneous squinted SAR acquisitions,” *IEEE Trans. Geosci. Remote Sens.*, vol. 56, no. 4, pp. 2147–2158, Apr. 2018.

[26] E. Mullen, “Space radiation environments for parts selection/test considerations in typical satellite orbits,” Assurance Technol. Corp., Carlisle, MA, USA, Tech. Rep. 1, 2003.

[27] H. H. Andersen, J. F. Bak, H. Knudsen, and B. R. Nielsen, “Stopping power of Al, Cu, Ag, and Au for MeV hydrogen, helium, and lithium ions. $Z_1^3$ and $Z_1^4$ proportional deviations from the Bethe,” *Phys. Rev. A, Gen. Phys.*, vol. 16, no. 5, p. 1929, 1977.

[28] M. Burrell, J. Watts, and J. Wright, “An analysis of energetic space radiation and dose rates,” NASA, Washington, DC, USA, Tech. Rep. TN D-4404, 1968.

[29] “Nuclear and space radiation effects on materials,” NASA, Washington, DC, USA, Tech. Rep. SP-8053, Jun. 1970.

[30] R. R. Bate, D. D. Mueller, and J. E. White, *Fundamentals of Astrodynamics*. Chelmsford, MA, USA: Courier Corporation, 1971.

[31] M. Turner, *Rocket and Spacecraft Propulsion: Principles, Practice and New Developments*. Springer, 2009.

[32] E. Perez, “Soyuz at the guiana space centre user’s manual—Revision 0,” Arianesp., Évry, France, Tech. Rep., 2012, no. 2.

[33] “Falcon 9 LEO, GTO and C3 performance,” Space Explor. Technol. Corp., Hawthorne, CA, USA, Tech. Rep., May 2016.

[34] R. Lagier, “Ariane 5 user’s manual—Revision 2,” Arianesp., Évry, France, Tech. Rep., 2016, no. 5.

[35] M. Naranjo *et al.*, “Biomass P-band SAR reflector antenna—Feed S/S breadboarding,” in *Proc. 10th Eur. Conf. Synth. Aperture Radar*, Jun. 2014, pp. 1–4.

[36] P. Valle, G. Orlando, R. Mizzoni, F. Hélière, and K. van’t Klooster, “P-band feedarray for BIOMASS,” in *Proc. 6th Eur. Conf. Antennas Propag.*, Mar. 2012, pp. 3426–3430.

[37] S. Huber, F. Q. de Almeida, M. Villano, M. Younis, G. Krieger, and A. Moreira, “Tandem-L: A technical perspective on future spaceborne SAR sensors for Earth observation,” *IEEE Trans. Geosci. Remote Sens.*, vol. 56, no. 8, pp. 4792–4807, Aug. 2018.

[38] G. Krieger, N. Gebert, M. Younis, F. Bordoni, A. Patyuchenko, and A. Moreira, “Advanced concepts for ultra-wide-swath SAR imaging,” in *Proc. EUSAR*, Friedrichshafen, Germany, Jun. 2008, pp. 1–4.

[39] G. Krieger *et al.*, “Advanced digital beamforming concepts for future SAR systems,” in *Proc. IEEE Int. Geosci. Remote Sens. Symp.*, Jul. 2010, pp. 245–248.

[40] M. Villano, G. Krieger, and A. Moreira, “Staggered SAR: High-resolution wide-swath imaging by continuous PRI variation,” *IEEE Trans. Geosci. Remote Sens.*, vol. 52, no. 7, pp. 4462–4479, Jul. 2014.

[41] W. Emery and A. Camps, *Introduction to Satellite Remote Sensing: Atmosphere, Ocean, Land and Cryosphere Applications*. Amsterdam, The Netherlands: Elsevier, 2017.


**Jalal Matar** was born in Lebanon in 1989. He received the B.S. degree (Hons.) in computer communication engineering from Notre Dame University–Louaize, Zouk Mosbeh, Lebanon, in 2012, and the M.S. degree in communications technology from Ulm University, Ulm, Germany, in 2014. He is currently pursuing the Dr.-Ing. (Ph.D.) degree in electrical engineering with the Karlsruhe Institute of Technology (KIT), Karlsruhe, Germany.

Since September 2014, he has been with the Microwaves and Radar Institute, German Aerospace Center (DLR), Weßling, Germany, as a Research Scientist. His research interests include the study and design of future synthetic aperture radar (SAR) mission concepts, especially high-altitude spaceborne systems at medium Earth orbit altitudes.

**Marc Rodriguez-Cassola** was born in Barcelona, Spain, in 1977. He received the Ingeniero degree in telecommunication engineering from the Universidad Publica de Navarra, Pamplona, Spain, in 2000, the Licenciado (M.Sc.) degree in economics from the Universidad Nacional de Educación a Distancia, Madrid, Spain, in 2012, and the Ph.D. degree in electrical engineering from the Karlsruhe Institute of Technology, Karlsruhe, Germany, in 2012.

From 2000 to 2001, he was a Radar Hardware Engineer with CETP/CNRS, Saint-Maur-des-Fossés, France. From 2001 to 2003, he was a Software Engineer with Altran Consulting, Munich, Germany. Since 2003, he has been with the Microwaves and Radar Institute, German Aerospace Center, Weßling, Germany, where he is currently leading the SAR Missions Group. His research interests include radar signal processing, synthetic aperture radar (SAR) end-to-end simulation, SAR processing and calibration algorithms, crisis theory, and radar mission analysis and applications.

**Gerhard Krieger** (M'04–SM'09–F'13) received the Dipl.-Ing. (M.S.) and Dr.-Ing. (Ph.D.) (Hons.) degrees in electrical and communication engineering from the Technical University of Munich, Munich, Germany, in 1992 and 1999, respectively.

From 1992 to 1999, he was with Ludwig Maximilians University, Munich, where he conducted multidisciplinary research on neuronal modeling and nonlinear information processing in biological and technical vision systems. Since 1999, he has been with the Microwaves and Radar Institute, German Aerospace Center (DLR), Weßling, Germany, where he started as a Research Associate developing signal processing algorithms for a novel forward-looking radar system employing digital beamforming on receive. From 2001 to 2007, he led the New SAR Missions Group, DLR, which pioneered the development of advanced bistatic and multistatic radar systems, such as TanDEM-X, as well as innovative multichannel synthetic aperture radar (SAR) techniques and algorithms for high-resolution wide-swath SAR imaging. Since 2008, he has been the Head of the Radar Concepts Department, DLR, which hosts about 40 scientists focusing on new SAR techniques, missions, and applications. Since 2006, he has been serving as a Mission Engineer for TanDEM-X and he also made major contributions to the development of Tandem-L, where he led the Phase-0 and Phase-A studies from 2008 to 2016 and is currently heading the mission and performance engineering activities. He holds a professorship at Friedrich-Alexander-University Erlangen, Erlangen, Germany. He has authored or coauthored more than 90 peer-reviewed journal articles, 9 invited book chapters, and about 400 conference articles. He holds more than 15 patents.

Dr. Krieger was a recipient of received several national and international awards, including the W. R. G. Baker Prize Paper Award from the IEEE Board of Directors, two Best Paper Awards at the European Conference on Synthetic Aperture Radar, and two Transactions Prize Paper Awards of the IEEE Geoscience and Remote Sensing Society. He served as the Technical Program Chair for the European Conference on Synthetic Aperture Radar and as a Guest Editor for the IEEE JOURNAL OF SELECTED TOPICS IN APPLIED EARTH OBSERVATIONS AND REMOTE SENSING in 2014. He has been an Associate Editor for the IEEE TRANSACTIONS ON GEOSCIENCE AND REMOTE SENSING since 2012.

**Paco López-Dekker** (S'98–M'03–SM'14) was born in Nijmegen, The Netherlands, in 1972. He received the Ingeniero degree in telecommunication engineering from the Universitat Politécnica de Catalunya (UPC), Barcelona, Spain, in 1997, the M.S. degree in electrical and computer engineering from the University of California at Irvine, Irvine, CA, USA, in 1998, under the Balsells Fellowship, and the Ph.D. degree from the University of Massachusetts Amherst, Amherst, MA, USA, in 2003, with a focus on clear-air imaging radar systems to study the atmospheric boundary layer.

From 1999 to 2003, he was with the Microwave Remote Sensing Laboratory, University of Massachusetts Amherst. In 2003, he was with the Starlab, Barcelona, where he was involved in the development of GNSS-R sensors. From 2004 to 2006, he was a Visiting Professor with the Department of Telecommunications and Systems Engineering, Universitat Autonoma de Barcelona, Barcelona. In 2006, he joined the Remote Sensing Laboratory, UPC, where he conducted the research on bistatic synthetic aperture radar (SAR) under a 5-year Ramon y Cajal Grant. From 2009 to 2016, he led the SAR Missions Group, Microwaves and Radar Institute, German Aerospace Center, Weßling, Germany. The focus of the SAR Missions Group was the study of future SAR missions, including the development of novel mission concepts and detailed mission performance analyses. Since 2016, he has been an Associate Professor with the Faculty of Civil Engineering and Geosciences, Delft University of Technology, Delft, The Netherlands. He is currently a Lead Investigator for the STEREOID Earth Explorer 10 mission candidate. His research interests include (In)SAR time series analysis, retrieval from ocean surface currents from radar data, and the development of distributed multistatic radar concepts.

**Alberto Moreira** (M'92–S'96–F'04) received the B.S.E.E. and M.S.E.E. degrees from the Aeronautical Technological Institute (ITA), São José dos Campos, Brazil, in 1984 and 1986, respectively, and the Eng.Dr. degree (Hons.) from the Technical University of Munich, Munich, Germany, in 1993.

From 1996 to 2001, he was the Chief Scientist and the Engineer with the SAR Technology Department, German Aerospace Center (DLR), Weßling, Germany. Under his leadership, the DLR airborne synthetic aperture radar (SAR) system has been upgraded to operate in innovative imaging modes like polarimetric SAR interferometry and SAR tomography. Since 2001, he has been the Director of the Microwaves and Radar Institute, DLR, and a Full Professor with the Karlsruhe Institute of Technology (KIT), Karlsruhe, Germany, in the field of microwave remote sensing. His DLR's Institute contributes to several scientific programs and projects for spaceborne SAR missions like TerraSAR?X, TanDEM?X, SAR?Lupe, and SARah as well as Kompsat-6, PAZ, Sentinel?1, BIOMASS, and Tandem?L. The mission TanDEM?X, led by his Institute, has generated a global, high-resolution digital elevation model of the Earth with unprecedented accuracy. He is the Initiator and Principal Investigator (PI) for this mission. He has authored or coauthored more than 400 publications in international conferences and journals and 8 book chapters. He holds 41 international patent grants in the radar and antenna field. His research interests include spaceborne radar end?to?end system design, microwave techniques and system concepts, signal processing, and remote sensing applications.

Dr. Moreira has served as the President for the IEEE Geoscience and Remote Sensing Society (GRSS) in 2010. He was a Founder and the Chair of the GRSS German Chapter from 2003 to 2008, served as an Associate Editor for IEEE GEOSCIENCE AND REMOTE SENSING LETTERS from 2003 to 2007 and for the IEEE TRANSACTIONS ON GEOSCIENCE AND REMOTE SENSING since 2005, and has been serving as the Chair for the Major Awards of the GRSS since 2017. He was a recipient of several international awards, including the IEEE AESS Nathanson Award in 1999 for the Young Radar Engineer of the Year, the IEEE Kiyo Tomiyasu Field Award in 2007, the IEEE W. R. G. Baker Award from the IEEE Board of Directors in 2012, and the IEEE GRSS Distinguished Achievement Award in 2014. He and his colleagues received the GRSS Transactions Prize Paper Awards in 1997, 2001, and 2007 and the GRSS Letters Prize Paper Award in 2015 and 2017. From 2012 to 2017, he has served as a Principal Investigator for the Helmholtz Alliance Remote Sensing and Earth System Dynamics and is currently the PI for Tandem-L, a radar mission proposal for the global observation of dynamic processes on the Earth's surface with unprecedented quality and resolution.